# *Electro-chemo-mechanical studies of perovskite-structured mixed ionic-electronic conducting SrSn[subscript 1-x]Fe[subscript x]O[subscript 3-x/2+#] part II: Electrical conductivity and cathode performance*



**Citation:** Kim, Chang Sub, et al. "Electro-chemo-mechanical studies of perovskite-structured mixed ionic-electronic conducting SrSn[subscript 1-x]Fe[subscript x]O[subscript 3-x/subscript 2+δ] part II: Electrical conductivity and cathode performance." Journal of Electroceramics, vol. 40, no. 1, Feb. 2018, pp. 57–64.

**As Published:** http://dx.doi.org/10.1007/s10832-017-0098-6

**Publisher:** Springer US

**Persistent URL:** http://hdl.handle.net/1721.1/116126

**Version:** Author's final manuscript: final author's manuscript post peer review, without publisher's formatting or copy editing

**170**

# Electro-chemo-mechanical Studies of Perovskite-Structured Mixed Ionic-Electronic Conducting $SrSn_{1-x}Fe_xO_{3-x/2+\delta}$ Part II: Electrical Conductivity and Cathode Performance

Chang Sub Kim[1], Sean R. Bishop[1,2.3], Harry L. Tuller[1,2,3]
[1]Department of Materials Science and Engineering, Massachusetts Institute of Technology, Cambridge, MA 02139, USA
[2]Materials Processing Center, Massachusetts Institute of Technology, Cambridge, MA 02139, USA
[3] International Institute for Carbon-Neutral Energy Research (WPI-I$^2$CNER), Kyushu University, Fukuoka 819-0395, Japan

ABSTRACT

The bulk electrical conductivity of the mixed ionic-electronic conducting perovskite-structured $SrSn_{1-x}Fe_xO_{3-x/2+\delta}$ (SSF) was measured to examine how changes in defect chemistry and electronic band structure associated with the substitution of Ti by Sn impact defect charge carrier density and ultimately electrode performance. These results complement a defect chemical model for SSF investigated and reported in Part I of this study. The electrical properties of SSF were found not to differ significantly from the corresponding composition in $SrTi_{1-x}Fe_xO_{3-x/2+\delta}$ (STF). It is believed that Fe dominates the character of the valence and conduction bands and thus governs the electronic properties in SSF. Though slightly shifted in energy due to the larger size of Sn, the defect equilibria and therefore the electrical conductivity of SSF were found to be largely dominated by Fe and thus differed only in a limited way from that in STF. Key kinetic parameters obtained include the migration enthalpy of oxygen vacancies (0.772±0.204 eV), the activation energy of area-specific-resistance for oxygen exchange (1.65±0.03 eV) and the magnitudes of electron (0.0002±0.00005 $cm^2/V{\cdot}s$) and hole (0.0037±0.0015 $cm^2/V{\cdot}s$) mobilities.

## Introduction

The high energy conversion efficiency and fuel flexibility of solid oxide fuel cells (SOFCs) make them attractive alternatives for generating electricity from chemical fuels. A great deal of recent attention in this field has been directed towards reducing the operating temperature of SOFC systems, requiring materials with considerably faster surface reaction kinetics, particularly at the cathode, leading to reduced area specific resistances. Towards this end, we have undertaken an investigation of oxygen deficient, mixed ionic-electronic conducting perovskite materials with formula $SrM_{1-x}Fe_xO_{3-x/2+\delta}$ (M = Ti, Sn).

In our previous studies, the mixed ionic and electronic conducting (MIEC) perovskite-structured $SrTi_{1-x}Fe_xO_{3-x/2+\delta}$ (STF) materials system was identified as a promising candidate for SOFC cathodes given rapid oxygen surface exchange kinetics, due in part to the simultaneous presence of ionic and electronic conductivity (i.e. mixed ionic electronic conduction [MIEC]) [1][2]. The exchange kinetics of STF were found to correlate with the minority electron charge density, n [1]. Studies were initiated on the closely related $SrSn_{1-x}Fe_xO_{3-x/2+\delta}$ (SSF) system to examine the possible role of the electron mobility in influencing the ASR. In Part I of this study [3], we found that the defect equilibria changed little upon substitution of Sn for Ti, given the key role of the redox flexible Fe in influencing defect formation via oxidation/reduction reactions. In Part II of this study, we here investigate whether, the Sn 5s derived energy band, characterized by high electron mobility [4][5], that replaces the narrower Ti 3d derived band in STF as the conduction band, leads to a considerable increase in electron mobility in SSF and thereby decreased ASR.

While there have been studies relating to the crystal structure and electrical properties of SSF previously by Thangadurai et. al. [6][7], their studies were limited to either highly reducing or oxidizing

oxygen partial pressure ($pO_2$) regimes. The electrical properties in the intermediate $pO_2$ regime, where the ionic conduction is expected to be dominant, were missing, as well as information about the electron and hole mobilities. In this work, the electrical properties of SSF materials are correlated with the defect chemical model reported in Part I of this study and are used to derive the ionic conductivity as well as the electronic carrier mobilities. Finally, the ASR of thin film SSF electrodes deposited onto single crystal yttria stabilized zirconia (YSZ) substrates are evaluated over a range of temperatures and compared to those of STF electrodes. Surprisingly, the performance of the SSF and STF materials is found to be quite similar. We discuss why this might be the case based on the defect and electronic structures of the two materials systems.

**Theory**

The defect chemistries of SSF and STF were described and evaluated in previous studies [3][8], a summary is provided below. The oxygen nonstoichiometry is written as $3-\frac{x}{2}+\delta$ where x is the Fe B-site fraction. Built-in oxygen deficiency is *x/2* due to the difference in valence states between the nominally $Fe^{3+}$ and the $Sn^{4+}$ or $Ti^{4+}$ B-site ions under cathodic operating conditions [8][9]. As a consequence, the insertion of extra oxygen into these normally unoccupied sites is denoted as creating 'interstitials'. This is described in terms of anion Frenkel disorder with the reaction written in Kröger–Vink notation as [8]:

$$O_O^x + V_i^x \leftrightarrow V_O^{\cdot\cdot} + O_i'' \tag{1}$$

where $O_O^x$ is an oxygen on an oxygen site with no net charge with respect to the lattice, $V_i^x$ is a charge neutral vacancy on an interstitial site (built-in oxygen deficiency), $V_O^{\cdot\cdot}$ is a vacancy on an oxygen site with two positive charges relative to the lattice, and $O_i''$ is an oxygen ion on an interstitial site with two negative charges relative to the lattice. Full ionization of the ionic defects is assumed, as is reasonable given the temperature range under study. The equilibrium constant can be written as

$$K'_{af} = \frac{[V_O^{\cdot\cdot}][O_i'']}{[O_O^x][V_i^x]} \tag{2}$$

Provided $[V_O^{\cdot\cdot}]$ and $[O_i'']$ remains small relative to $[O_O^x]$ and $[V_i^x]$, the latter can be assumed to remain approximately constant, and it becomes convenient to introduce a new constant $K_{af}$ given by,

$$K_{af} = K'_{af}[O_O^x][V_i^x] = [V_O^{\cdot\cdot}][O_i''] = K_{af}^0\, e^{-\frac{H_{af}}{kT}} \tag{3}$$

Intrinsic electron-hole pair generation can be written as:

$$\text{nil} \leftrightarrow e' + h^{\cdot} \tag{4}$$

and the equilibrium constant $K_i$ as

$$K_i = np = N_C N_V e^{-E_g/kT} \tag{5}$$

where $n$ and $p$ are the concentrations of electrons and holes in the conduction and valence bands, respectively, and $N_C$ and $N_V$ are effective density of conduction and valence band states, respectively.

Similarly, the oxygen reduction reaction can be described by the following reaction and equilibrium constant, $K'_{red}$:

$$O_O^x \leftrightarrow V_O^{\cdot\cdot} + 2e' + \frac{1}{2}O_2 \tag{6}$$

$$K'_{red} = \frac{[V_O^{\cdot\cdot}]n^2(pO_2)^{\frac{1}{2}}}{[O_O^x]} \tag{7}$$

As for the anion Frenkel equation above, provided $[V_O^{\cdot\cdot}]$ is much lower in magnitude than $[O_O^x]$, the latter can be treated as a constant, and the defect equations simplified as below.

$$K_{red} = K'_{red}[O_O^x] = K_{red}^0 e^{-\frac{H_{red}}{kT}} \tag{8}$$

By combining the three equilibrium constant equations – Equations (3), (5), and (8) – each defect carrier concentration can be expressed in terms of the three equilibrium constants, oxygen partial pressure, and intrinsic carrier concentration.

**Experimental**

*Bulk samples*

SSF solid solutions were prepared by the ball milling method. Strontium carbonate (Alfa Aesar, 99.99%), tin (IV) oxide (Alfa Aesar, 99.9%), and iron (III) oxide (Alfa Aesar, 99.945%) powders were mixed in the desired Sr/Sn/Fe ratios, ball milled with deionized water and ethanol for six hours, dried, and calcined in air at 1300 °C for six hours. The orthorhombically distorted perovskite phase was confirmed by powder X-ray diffraction (XRD). Two different shapes of bulk samples were prepared. A cylindrical sample was prepared to serve as a pulsed laser deposition (PLD) target, and a rectangular bar sample was prepared for bulk conductivity and chemical expansion studies, the latter discussed in a future publication. The prepared powders were placed in either a cylindrical or rectangular bar shaped stainless steel die, uniaxially pressed at 20 MPa for two minutes, and then sintered for six hours in air at 1500 °C. The density of the bulk samples was obtained by applying Archimedes' principle. The weight of the samples in air and in water were measured, and the relative density of the bulk samples were calculated to be approximately 97%.

*Thin film samples*

STF and SSF thin films were prepared by means of PLD (Neocera Inc., Beltsville, MD). After loading (001) oriented YSZ single crystal substrates (10×10×0.5 $mm^3$) from MTI Corporation (Richmond, CA) and a bulk target of desired composition, the PLD chamber was pumped down to a base pressure of $9\times10^{-6}$ Torr, and then the substrate was heated to 850 °C or 950 °C. The substrate temperature was calibrated to be about 150 °C lower than the heater temperature. A Coherent COMPex Pro 205 KrF excimer laser (Santa Clara, CA) of 248 nm wavelength with 400 mJ/pulse at 10 Hz was used to ablate STF and SSF targets. The surfaces of the targets were pre-ablated with 3,000 pulses before every deposition. The chamber was maintained at 10 mTorr oxygen pressure during deposition and 10 Torr after deposition, before cooling down to room temperature.

High resistances were observed within the film plane for both SSF and STF. Metal current collectors were therefore deposited between the thin films and the YSZ substrate. This facilitated lateral transport of the electronic carriers for through plane measurements to evaluate oxygen exchange, or oxygen reduction reaction (ORR), kinetics. Micro-patterns were fabricated using wideband ultraviolet photo-lithography. Patterns of 80 μm width/spacing were drawn using AutoCAD software and used to design a soda-lime glass base mask with chrome coating, custom-ordered from Advance Reproductions

Corporation (North Andover, MA). After spin-coating five drops of photoresist NR71-3000P (Futurex, Inc., Franklin, NJ) at 2,500 rpm for 30 seconds, samples were baked for two minutes at 160 °C and exposed to broadband ultraviolet light for 40 seconds through the chrome coated mask using a MA4 mask aligner (SUSS MicroTec, Garching, Germany). The samples were post-baked for two minutes at 105 °C and developed for two minutes (RD6, Futurex, Inc.). All samples were cleaned with oxygen plasma at 200 W in 0.5 Torr for three minutes to remove water molecules from the sample surface.

Dense Pt films were deposited on the photoresist patterned samples by DC sputtering (Kurt J. Lesker, Clairton, PA). After reaching a base pressure of $< 5\times10^{-6}$ Torr using a cryogenic pump (Cryotorr 8, CTI Cryogenics, Chelmsford, MA), DC power of 50 W was used to sputter Pt (10 mTorr of Ar) at room temperature. The lift-off process was completed by soaking the samples in a solvent (MICROSTRIP® 2001, FUJIFILM Electronics Materials U.S.A. Inc., North Kingstown, RI) for ten minutes at 100 °C to completely dissolve the photoresist.

*Bulk sample configuration*

Rectangular bar-shaped SSF bulk samples were prepared with dimensions of $21\times2.7\times2.47$ mm$^3$. Four sets of Pt wires were wrapped around the bars as illustrated in Figure 1. Pt paste was used to ensure good adhesion of the wires. The Pt pasted areas were approximately 3.17 mm wide and spaced 2.93 mm apart.

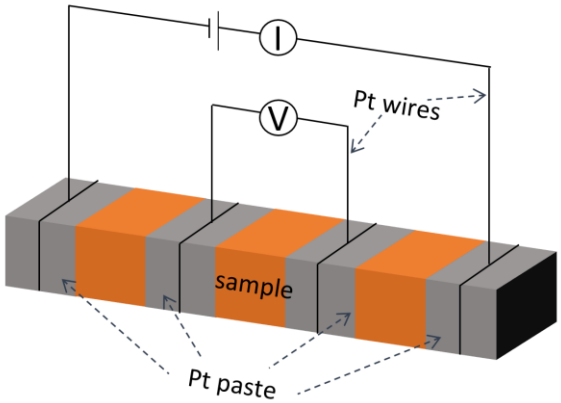


**Figure 1. A Schematic illustration of the SSF bulk sample with four-point probe setup for conductivity measurements.**

*Measurement conditions*

Conductivity measurements were performed at 700~1000 °C over a wide range of oxygen partial pressure ($10^{-20}$ ~ 1 atm) controlled by $O_2$-$N_2$ (high $pO_2$), $H_2$-$H_2O$-$N_2$ (low $pO_2$), and CO-$CO_2$ (intermediate $pO_2$) gas mixtures with the aid of MKS Instruments M100B (Andover, MA) MFCs. The oxygen pressure was monitored using an *in situ* Nernst based YSZ sensor. Four-point impedance measurements was measured by HP 4192A over a frequency range 5 Hz ~ 13 MHz.

*Thin film EIS measurements*

*Cell configuration*

Asymmetric cells were prepared by depositing SSF thin films by PLD over the patterned Pt current collectors on (001) oriented YSZ electrolytes. Porous Ag was painted to the other side of the YSZ to serve as a counter electrode as shown in Figure 2.

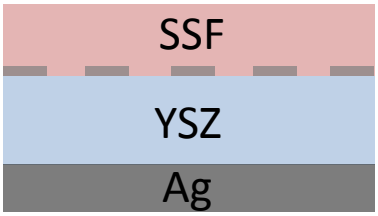


**Figure 2. Schematic illustrations of asymmetric cells with YSZ electrolyte, SSF working electrode with buried Pt current collector, and porous Ag counter electrode.**

*Measurement conditions*

Electrochemical impedance spectroscopy measurements were performed with a Modulab-MTS Test System (Solartron Analytical, Hampshire, UK). Samples were held by metal clips that were wrapped with 99.99% pure Pt wire (Alfa Aesar) and provided electrical contact. An AC amplitude of 10~20 mV and a frequency range from 3 mHz to 1 MHz were used during the study. A YSZ Nernst-type oxygen sensor, maintained at a constant temperature in a separate furnace connected to the sample furnace, served to monitor the oxygen partial pressure.

## Results

*Bulk conductivity*

The bulk conductivity of SSF35 is shown plotted vs $pO_2$ in a log-log plot in Figure 3 for a series of isotherms ranging from 700~1000 °C in one hundred degree intervals. The SSF35 exhibits p-type conductivity with a slope of 0.254 ± 0.017 under oxidizing conditions, a $pO_2$ insensitive ionic region at intermediate $pO_2$, and n-type conductivity with a -0.180 ± 0.007 slope under reducing conditions. This trend is similar to that exhibited by STF35, as shown in Figure 4.

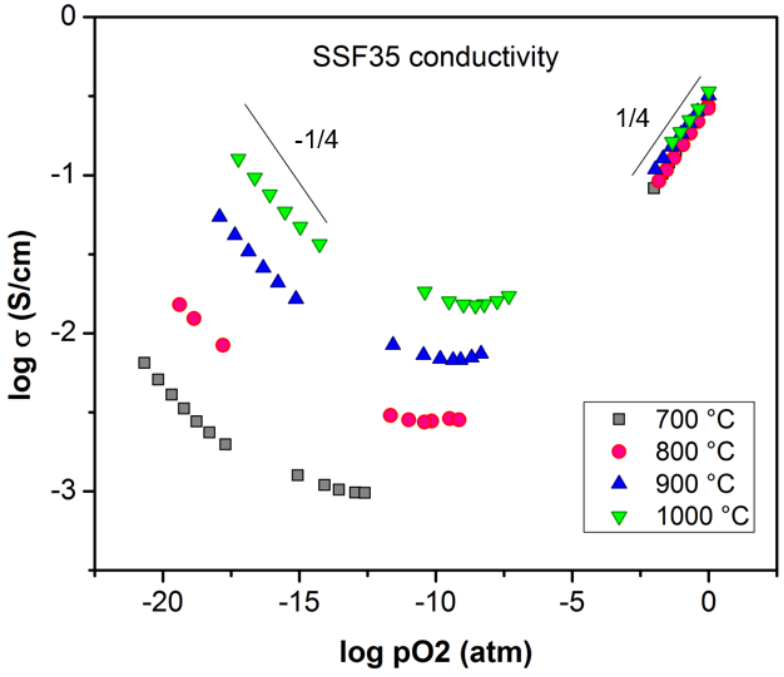


**Figure 3. Bulk electrical conductivity of SSF35 as a function of $pO_2$ and temperature.**

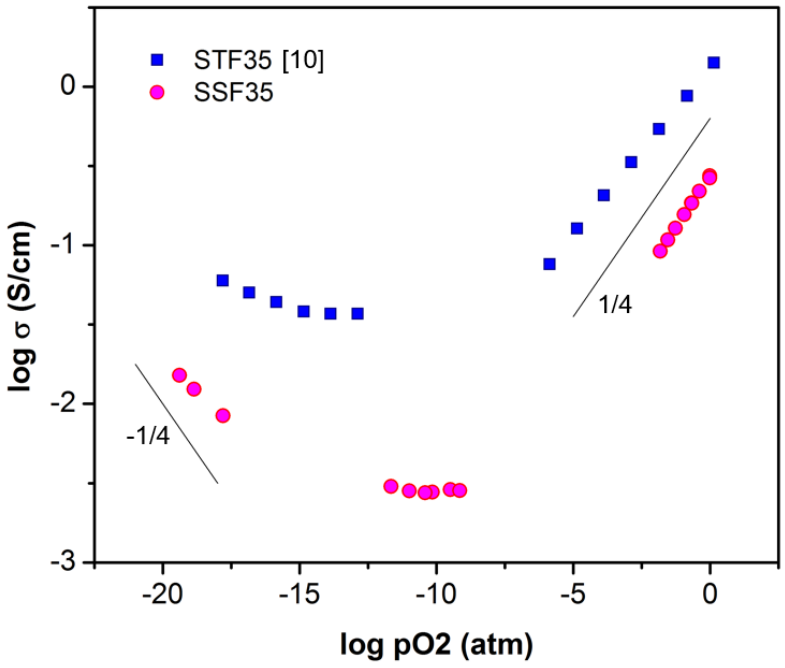


**Figure 4. Comparison of bulk conductivities of STF35** [10] **and SSF35 at 800°C.**

*EIS results of SSF thin film electrodes*

Figure 5 shows a typical impedance spectroscopy spectrum of the asymmetric cell. There is an offset resistance, independent of oxygen partial pressure, representing the ohmic resistance of the YSZ electrolyte, and a highly distorted semicircle in the high frequency domain showing very similar characteristics to porous Ag counter electrodes, as reported by Chen, et. al. in our group [11]. As also observed for STF 35 [1], the large, nearly ideal semicircle in the low frequency domain can be attributed to the SSF35 ASR or thin film surface exchange kinetics. The offset resistance, the Ag counter electrode ASR and the SSF ASR all show Arrhenius behavior. The diameter of the semicircle at low frequency, corresponding to the SSF35 electrode resistance, is normalized by the film area to give the area specific resistance (ASR) and is plotted against temperature in Figure 6. Also included are earlier results obtained for a STF35 thin film. The activation energies for the STF35 and SSF35 thin films are very similar at 1.70±0.04 eV and 1.65±0.03 eV, respectively.

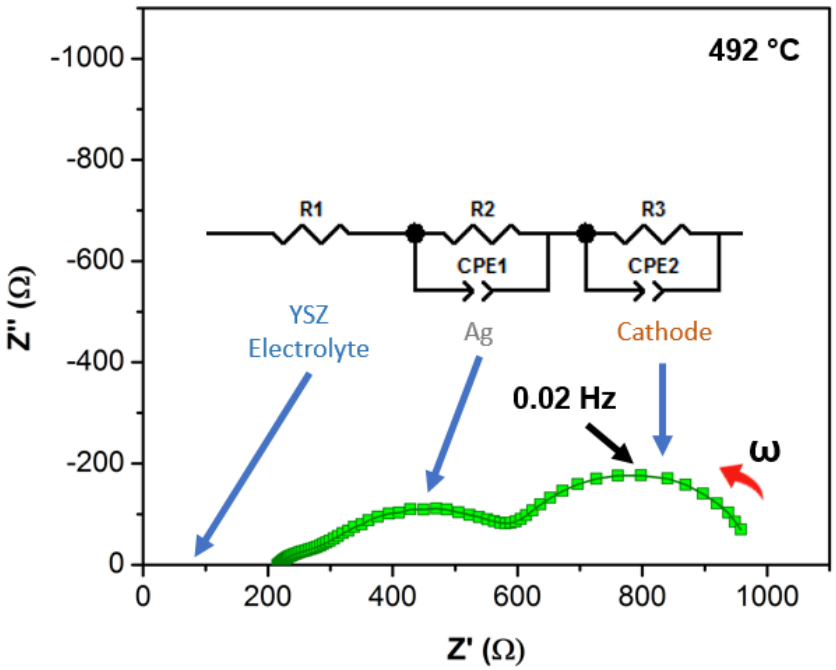


**Figure 5. Typical electrochemical impedance spectroscopy (EIS) spectrum of a SSF35 thin film deposited onto a single crystal YSZ electrolyte with buried Pt current collectors and porous Ag counter electrode at 492 °C.**

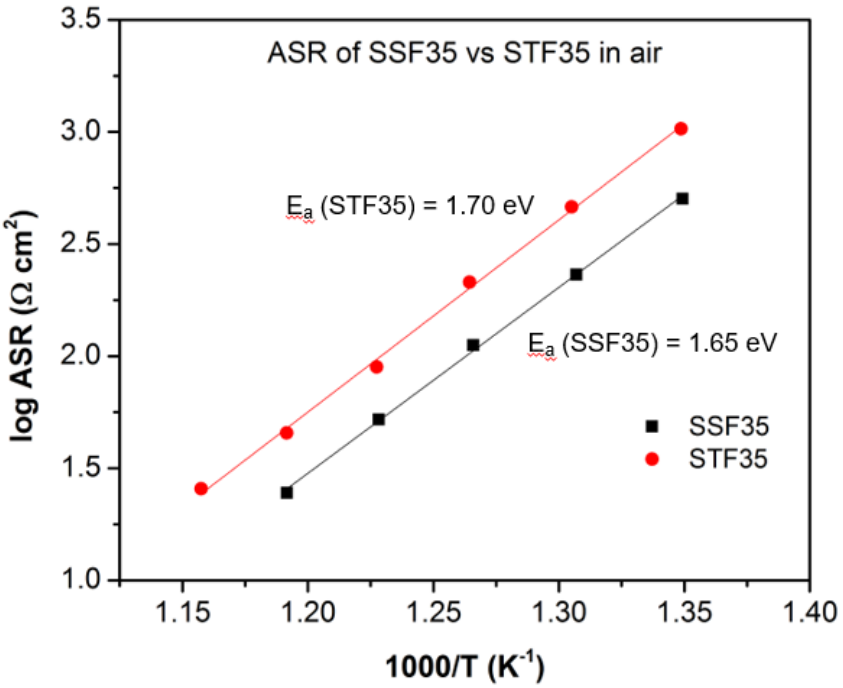


**Figure 6. Comparison of temperature dependence of area specific resistance (ASR) of SSF35 and STF35 thin film electrodes.**

**Discussion**

Four-point impedance measurements of SSF bulk samples showed a single semicircle in the frequency range of the instrument (HP 4192A, 5 Hz ~ 13 MHz). The sample resistance R was extracted by fitting the data to the equivalent parallel RC circuit and the conductivity $\sigma$ calculated taking into account the sample geometry, i.e. $\sigma = \frac{1}{R}\frac{\ell}{A}$ where $\ell$ is the distance between the voltage leads and $A$ the cross sectional area. A value for the $pO_2$ independent ionic conductivity was subtracted from the total conductivity in Figure 3. The extracted values for the n and p type contributions are shown plotted in Figure 7 as a function of $pO_2$ exhibiting slopes of 0.25±0.01 consistent with the expected defect model. The partial ionic, n and p type conductivities are next plotted vs reciprocal temperature in Figure 8 as log σT vs 1000/T at fixed $pO_2$ assuming thermally activated mobilities for all carriers of the form

$$\mu = \frac{\mathrm{A}}{\mathrm{T}} \exp\left(-\frac{E_a}{k\mathrm{T}}\right) \tag{9}$$

where A is a constant independent of temperature [12]. This choice, assuming small polaron hopping for the electronic carriers, is consistent with the low magnitudes of electron and hole mobilities derived below. The derived activation energies were found to be equal to $E_{a,\sigma_n \bullet \mathrm{T}} = 1.832 \pm 0.120$ eV, $E_{a,\sigma_p \bullet \mathrm{T}} = 0.048 \pm 0.032$ eV and $E_{a,\sigma_{ion} \bullet \mathrm{T}} = 1.042 \pm 0.029$ eV. The unusual nearly zero temperature coefficient of resistance (TCR) exhibited by SSF35 is similar to that found for STF35 and, as shown in the latter case, is a result of compensation of the expected positive TCR associated with mobility by the negative TCR associated with hole generation, for the special conditions where the Fermi energy lies close to the valence band edge [10].

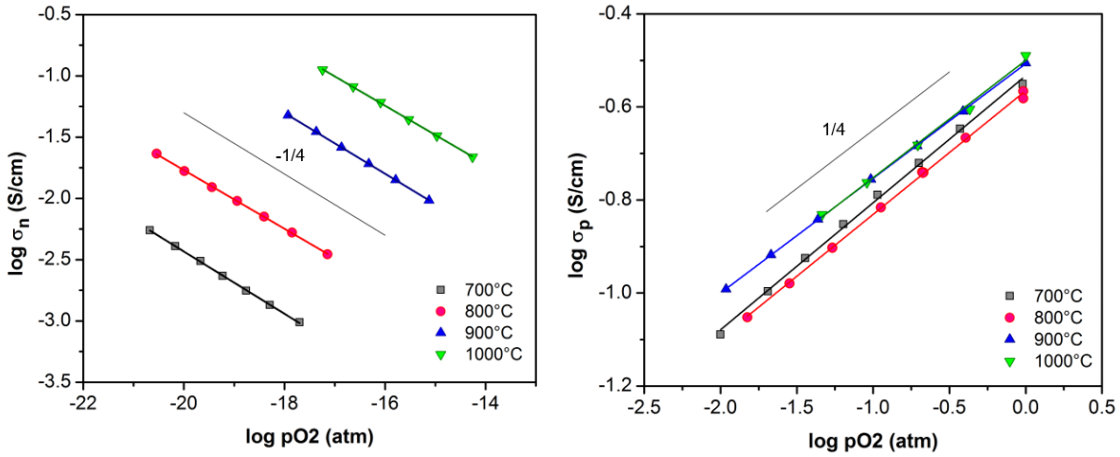


**Figure 7. Oxygen partial pressure dependence of (a) n-type and (b) p-type conductivities of SSF35 extracted by subtracting the respective ionic conductivities from the total conductivity at each isotherm.**

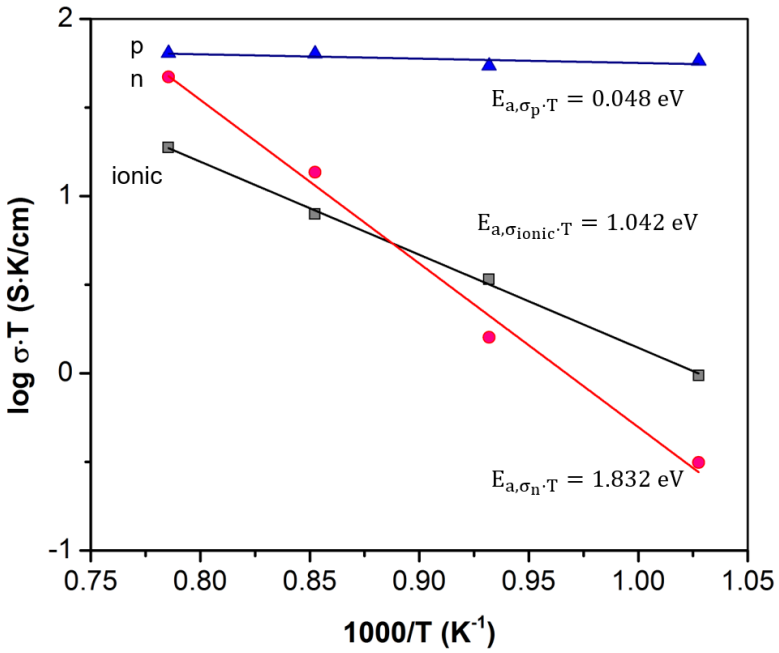


**Figure 8. Temperature dependence of p-type ($pO_2$ = 0.316 atm), n-type ($pO_2$ = $10^{-18}$ atm) , and $pO_2$-insensitive ionic conductivities of SSF35.**

Given expressions for the partial conductivities derived in this study and knowledge of the corresponding carrier densities obtained from the defect model derived in Part I of this study, it becomes possible to extract values for the corresponding carrier mobilities. The conductivity of a material is defined by

$$\sigma = \sum_i \sigma_i = \sum_i [i] q_i \mu_i \qquad (10)$$

where *i* refers to the i$^{th}$ charge carrier (electron, hole, or oxygen vacancy), $[i]$ is the concentration, $q_i$ is the charge and $\mu_i$ is the mobility of the carrier. The electronic carrier mobilities calculated by combining the conductivity data of this study with the previously derived defect model, are listed in Table 1 and are plotted vs reciprocal temperature in Figure 9.

In contrast to expectations of a much higher electron mobility in SSF, the electron mobility of SSF35 (~0.0002 cm$^2$/V·s) is found to be less than a quarter of that of STF35 (~0.0009 cm$^2$/V·s [8]). This suggests that the conduction band of SSF35 is dominated by the Fe 3d derived band, rather than the higher mobility Sn 5s derived band, which in case of $SnO_2$, gives a Hall mobility of approximately 50 cm$^2$/V·s at 625 K [13]. STF35 may have the higher mobility given that the Fe 3d orbital may be more heavily hybridized with Ti 3d, resulting in higher mobility than the more isolated Fe 3d derived band in SSF35 which lies much below the Sn 5s band (Figure 10). While the magnitude of the electron mobility is clearly in the small polaron regime (~ 3x10$^{-3}$ cm$^2$/V·s at 800 °C), our best fit to the mobility data nevertheless gives a very small negative slope (~-0.047 eV). We believe this is due to the difficulty in separating out the very small difference in activation energies for the electron density *n* derived from the defect model in Part 1 of this study [3] based on thermogravimetric data and the n-type conductivity in this study, both of which give steep activation energies on the order of 1.8 eV. In contrast to the situation for electrons, SSF35 (Table 1) and STF35 (0.005 cm$^2$/V·s [8]) show similar hole mobilities. This can be explained by similar valence band structure – Fe 3d and O 2p hydbridization – expected in both

SSF35 and STF35. The lower ionic mobility of SSF35 seems to be due to the differences in symmetry – close-to-tetragonal orthorhombic SSF35 structure compared to cubic STF35 structure.

**Table 1. Electron, hole, and ionic mobilities of SSF35 calculated from defect chemistry and conductivity data.**

| T (°C) | $\mu_n$ ($cm^2/V{\cdot}s$) | $\mu_p$ ($cm^2/V{\cdot}s$) | $\mu_{ion}$ ($cm^2/V{\cdot}s$) |
|---|---|---|---|
| 700 | 0.000252 | 0.00238 | $2.31\times10^{-6}$ |
| 800 | 0.000152 | 0.00291 | $5.86\times10^{-6}$ |
| 900 | 0.000215 | 0.00429 | $10.46\times10^{-6}$ |
| 1000 | 0.000204 | 0.00523 | $19.64\times10^{-6}$ |

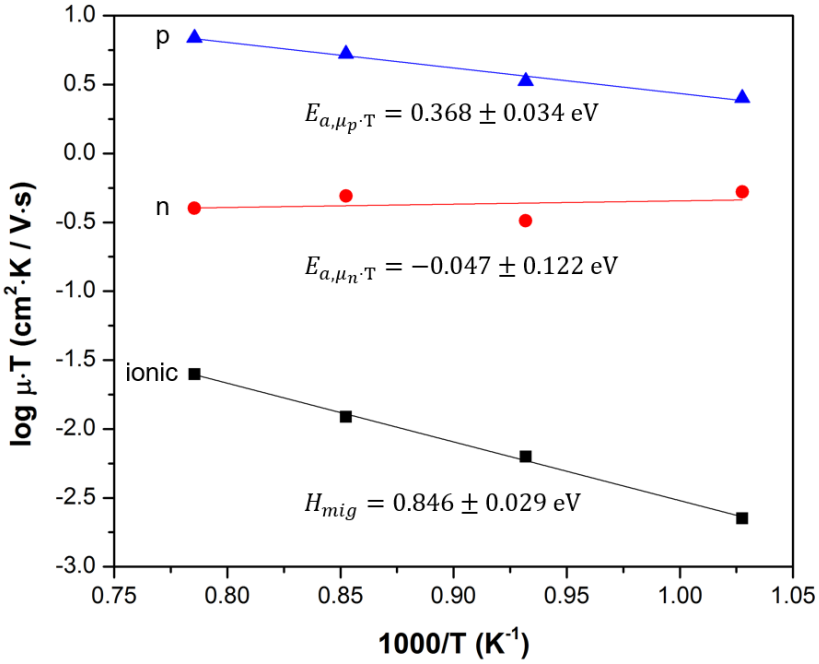


**Figure 9. Temperature dependence of electron and hole mobilities of SSF35.**

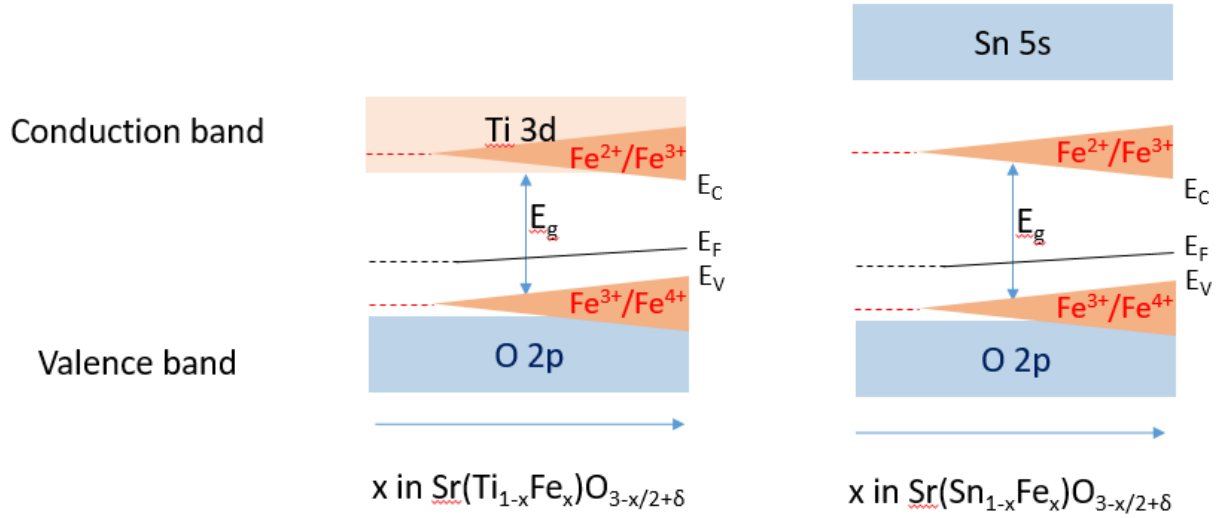


**Figure 10. Expected conduction and valance band positions of STF and SSF as a function of Fe content, *x*.**

As drawn in Figure 10, SSF has a larger bandgap compared to STF due to the higher level of the Sn 5s derived conduction band as compared to that of the Ti 3d band. This is observed both thermally [3] and optically [2][14]. The activation energies associated with each type of conductivity extracted from the slopes in Figure 8 represent the sum of the charge carrier formation and mobility (migration) activation energies. Therefore, by subtracting the activation energies related to electron and hole generations derived from Part I of this study, activation energies of electron and hole mobility were calculated and listed in Table 2 and Table 3. These values are slightly different from the slope obtained from Figure 9 due to different assumptions (values in the figure are from fixed $pO_2$ while the values in the tables are calculated from activation energies), but agree within the level of uncertainty.

**Table 2. Activation energies of n-type conductivity, electron concentration, and electron mobility.**

| $E_{a,\sigma_n \bullet T}$ | $E_{a,n}$ | $E_{a,\mu_n \bullet T}$ |
|---|---|---|
| 1.832 ± 0.120 eV | 1.961 ± 0.051 eV | -0.129 ± 0.171 eV |

**Table 3. Activation energies of p-type conductivity, hole concentration, and hole mobility.**

| $E_{a,\sigma_p \bullet T}$ | $E_{a,p}$ | $E_{a,\mu_p \bullet T}$ |
|---|---|---|
| 0.048 ± 0.032 eV | -0.217 ± 0.006 eV | 0.265 ± 0.038 eV |

An activation energy of hole conductivity for a nonstoichiometric oxide semiconductor of close to zero, i.e. $E_{a,\sigma_p \bullet T} = 0.048\ eV$, is highly unusual. However, as discussed above, a similar observation was already made previously for the related STF35 system. There it was shown that with the Fermi energy close to the valence band, $E_{a,p}$ took on a small positive value, while presumed phonon scattering resulted in a small effective negative value for $E_{a,\mu_p}$ which served to nearly compensate $E_{a,\mu_p}$ to result in a near zero value for $E_{a,\sigma_p}$[10]. This is likely the case here as well.

For the ionic component, the activation energy for oxygen vacancy formation was calculated from the defect model of SSF, i.e. $\frac{H_{af}}{2} = E_{a,[V_O^{\cdot\cdot}]}$, while the migration enthalpy $H_{mig}$ was obtained by subtracting that activation energy from the total ionic conductivity temperature product activation energy,

as shown in Table 4. Since $[O_i^{''}]$ represents oxygen in a structural vacancy site, there is no migration pathway for $[O_i^{''}]$, so $[V_O^{\cdot\cdot}]$ is the sole ionic transport species [15]. The calculated migration enthalpy of SSF35 is in the same range as other MIEC perovskite oxides (0.5~0.9 eV) [16].

**Table 4. Activation energies of ionic conductivity, oxygen vacancy concentration, and enthalpy of oxygen vacancy migration.**

| $E_{a,\sigma_{ion}\bullet T}$ | $E_{a,[V_O^{\cdot\cdot}]}$ | $H_{mig}$ |
|---|---|---|
| 1.042 ± 0.029 eV | 0.175 ± 0.175 eV | 0.867 ± 0.204 eV |

*Investigation of surface exchange kinetics of STF/SSF thin films*

The surface exchange coefficient *k* is inversely proportional to the area specific resistance (ASR) of STF/SSF thin films by the following equation [1][17]:

$$k = \frac{k_B T}{4e^2 R_S c_O} \tag{11}$$

where $k_B$ is the Boltzmann constant, $R_S$ is the area specific resistance, and $c_O$ is the total concentration of lattice oxygen; for $c_O$, a value of $4.92 \times 10^{22}$ cm$^{-3}$ and $4.67 \times 10^{22}$ cm$^{-3}$ was used for STF35 and SSF35, respectively in Figure 11.

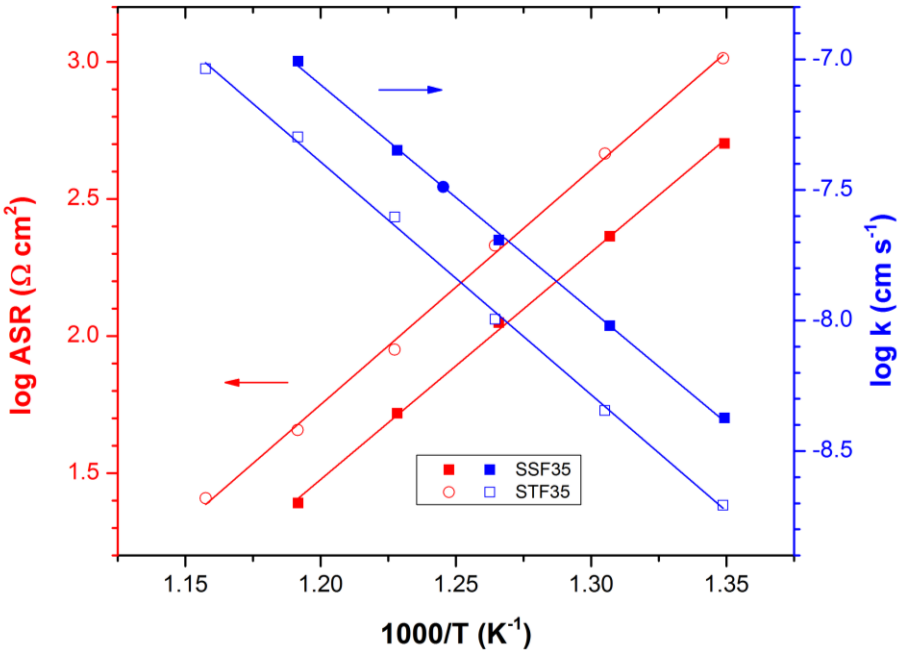


**Figure 11. Comparison of temperature dependence of area specific resistance (ASR) and surface exchange coefficient *k* of SSF35 and STF35 thin film electrodes.**

Though bulk properties may differ from that of corresponding thin films (due to e.g., lattice mismatch induced strain between film and substrate), bulk trends are good indicators for predicting corresponding properties in thin films. A strong correlation between *k* and the minority electron carrier density, *n*, was noted in [1]. SSF35 has slightly larger *n* as derived from the defect equilibrium model, but a lower

electron mobility. Interestingly, SSF35 showed slightly better surface exchange kinetics, and nearly the identical activation energy for ASR (or *k*) (Figure 11). This is not inconsistent with the hypothesis that the electrons in the conduction band are rate limiting in the oxygen surface exchange reaction. From part 1 of this series, the defect equilibria of SSF showed almost identical behavior as STF, but with slightly higher *n* at a given oxygen partial pressure.

## CONCLUSIONS

The electrical properties of a new SOFC model cathode material $SrSn_{1-x}Fe_xO_{3-x/2+\delta}$ have been explored in this study. The partial electronic and ionic conductivities of SSF35 were determined for SSF35 with key parameters derived, namely the migration enthalpy of oxygen vacancies (0.772±0.204 eV), and the electron (0.0002±0.00005 $cm^2/V{\cdot}s$) and hole (0.0037±0.0015 $cm^2/V{\cdot}s$) mobilities.

The n-type electrical conductivity of SSF35 followed the same trend as its STF counterpart, but with lower magnitude, suggesting that the Fe 3d band is largely responsible for electron conduction in the conduction band rather than the wider Sn 5s band. STF35 showed higher electron mobility, possibly due to the Ti 3d derived band hybridizing more extensively with the Fe 3d derived band, while only the Fe 3d derived band is involved in supporting electron transport in SSF35. The hole mobility of SSF35, on the other hand, was close in magnitude to that of STF35, as might be expected, given that hybridized Fe 3d and O 2p orbitals constitute the valence bands of both SSF35 and STF35.

The surface exchange rate and its activation energy for SSF35 were similar to those of STF35. SSF35's higher electron density in the conduction band seems to be compensated by its lower electron mobility in terms of the magnitude of the n-type conductivity. Moreover, Sr segregates to the surface of STF35 while both also depend on Fe for charge transfer. It would thus be interesting to study surface segregation in SSF and see how it compares with that in STF [18]. Surface exchange kinetics were found to be strongly dependent on surface termination in metal oxides, such as $SnO_2$ [19]. Surface segregation has been considered as one of the major issues for SOFC cathodes at high temperatures and in long term operations [18][20][21][22].


### Acknowledgments

This research was carried out as a part of the activity of the Skoltech-MIT Center for Electrochemical Energy Storage. Some of the concepts applied in this study on SSF were developed previously in research supported by the National Science Foundation under award number DMR-1507047.


## REFERENCES


[1] W. Jung and H. L. Tuller, "A New Model Describing Solid Oxide Fuel Cell Cathode Kinetics: Model Thin Film $SrTi_{1-x}Fe_xO_{3-\delta}$ Mixed Conducting Oxides–a Case Study," *Adv. Energy Mater.*, vol. 1, pp. 1184–1191, 2011.

[2] A. Rothschild, W. Menesklou, H. L. Tuller, and E. Ivers-Tiffée, "Electronic Structure, Defect Chemistry, and Transport Properties of $SrTi_{1-x}Fe_xO_{3-y}$ Solid Solutions," *Chem. Mater.*, vol. 18, no. 16, pp. 3651–3659, 2006.

[3] C. S. Kim, S. R. Bishop, N. H. Perry, and H. L. Tuller, "Electro-chemo-mechanical studies of perovskite-structured mixed ionic-electronic conducting $SrSn_{1-x}Fe_xO_{3-x/2+\delta}$ part I: Defect chemistry," *J. Electroceramics*, Jan. 2017.

[4] H. J. Kim, U. Kim, T. H. Kim, J. Kim, H. M. Kim, B. G. Jeon, W. J. Lee, H. S. Mun, K. T. Hong,

J. Yu, K. Char, and K. H. Kim, "Physical properties of transparent perovskite oxides (Ba,La)SnO 3 with high electrical mobility at room temperature," *Phys. Rev. B - Condens. Matter Mater. Phys.*, vol. 86, no. 16, pp. 1–9, 2012.

[5] D. J. Singh, D. A. Papaconstantopoulos, J. P. Julien, and F. Cyrot-Lackmann, "Electronic structure of Ba(Sn,Sb) O3: Absence of superconductivity," *Phys. Rev. B*, vol. 44, no. 17, pp. 9519–9523, 1991.

[6] V. Thangadurai, P. Schmid Beurmann, and W. Weppner, "Mixed oxide ion and electronic conductivity in perovskite-type $SrSnO_3$ by Fe substitution," *Mater. Sci. Eng. B*, vol. 100, no. 1, pp. 18–22, 2003.

[7] V. Thangadurai, R. A. Huggins, and W. Weppner, "Use of simple ac technique to determine the ionic and electronic conductivities in pure and Fe-substituted $SrSnO_3$ perovskites," *J. Power Sources*, vol. 108, no. 1–2, pp. 64–69, 2002.

[8] M. Kuhn, J. J. Kim, S. R. Bishop, and H. L. Tuller, "Oxygen Nonstoichiometry and Defect Chemistry of Perovskite-Structured $Ba_xSr_{1-x}Ti_{1-y}Fe_yO_{3-y/2+\delta}$ Solid Solutions," *Chem. Mater.*, vol. 25, no. 15, pp. 2970–2975, 2013.

[9] K. S. Roh, K. H. Ryu, and C. H. Yo, "Nonstoichiometry and Physical Properties of the $SrSn_{1-x}Fe_xO_{3-y}$System," *J. Solid State Chem.*, vol. 142, no. 2, pp. 288–293, 1999.

[10] A. Rothschild, S. J. Litzelman, H. L. Tuller, W. Menesklou, T. Schneider, and E. Ivers-Tiffée, "Temperature-independent resistive oxygen sensors based on $SrTi_{1-x}Fe_xO_{3-\delta}$ solid solutions," *Sensors Actuators, B Chem.*, vol. 108, no. 1–2 SPEC. ISS., pp. 223–230, 2005.

[11] D. Chen, S. R. Bishop, and H. L. Tuller, "Praseodymium-cerium oxide thin film cathodes: Study of oxygen reduction reaction kinetics," *J. Electroceramics*, vol. 28, no. 1, pp. 62–69, 2012.

[12] H. L. Tuller and A. S. Nowick, "Small polaron electron transport in reduced CeO2 single crystals," *J. Phys. Chem. Solids*, vol. 38, no. 8, pp. 859–867, 1977.

[13] C. G. Fonstad and R. H. Rediker, "Electrical properties of high-quality stannic oxide crystals," *J. Appl. Phys.*, vol. 42, no. 7, pp. 2911–2918, 1971.

[14] Q. Liu, H. Li, B. Li, W. Wang, Q. Liu, Y. Zhang, and J. Dai, "Structure and band gap engineering of Fe-doped SrSnO 3 epitaxial films," *EPL (Europhysics Lett.*, vol. 108, no. 3, p. 37003, 2014.

[15] V. Metlenko, W. Jung, S. R. Bishop, H. L. Tuller, and R. A. De Souza, "Oxygen diffusion and surface exchange in the mixed conducting oxides $SrTi_{1-y}Fe_yO_{3-\delta}$," *Submitt. under Rev.*

[16] M. Cherry, M. S. Islam, and C. R. A. Catlow, "Oxygen Ion Migration in Perovskite-Type Oxides," *J. Solid State Chem.*, vol. 118, no. 1, pp. 125–132, Aug. 1995.

[17] F. Baumann, J. Fleig, H. Habermeier, and J. Maier, "Impedance spectroscopic study on well-defined (La,Sr)(Co,Fe)$O_{3-\delta}$ model electrodes," *Solid State Ionics*, vol. 177, no. 11–12, pp. 1071–1081, Apr. 2006.

[18] W. Jung and H. L. Tuller, "Investigation of surface Sr segregation in model thin film solid oxide fuel cell perovskite electrodes," *Energy Environ. Sci.*, vol. 5, no. 1, p. 5370, 2012.

[19] C. Körber, A. Wachau, P. Agoston, K. Albe, and A. Klein, "Self-limited oxygen exchange kinetics at $SnO_2$ surfaces.," *Phys. Chem. Chem. Phys.*, vol. 13, no. 8, pp. 3223–3226, 2011.

[20] W. Lee, J. W. Han, Y. Chen, Z. Cai, and B. Yildiz, "Cation size mismatch and charge interactions drive dopant segregation at the surfaces of manganite perovskites.," *J. Am. Chem. Soc.*, vol. 135, no. 21, pp. 7909–25, May 2013.

[21] K.-C. Chang, P. Fuoss, Y. Hoydoo, S. Gopalan, D. Ding, L. Meilin, B. Yildiz, and K. Gerdes, "Recent Solid Oxide Fuel Cell Cathode Studies," p. 159, 2013.

[22] N. Caillol, M. Pijolat, and E. Siebert, “Investigation of chemisorbed oxygen, surface segregation and effect of post-treatments on $La_{0.8}Sr_{0.2}MnO_3$ powder and screen-printed layers for solid oxide fuel cell cathodes,” *Appl. Surf. Sci.*, vol. 253, no. 10, pp. 4641–4648, 2007.